New Phytologist

Combined NanoSIMS and synchrotron X-ray fluorescence reveal distinct cellular and subcellular distribution patterns of trace elements in rice tissues

Katie L. Moore[1], Yi Chen[2], Allison M. L. van de Meene[2], Louise Hughes[3], Wenju Liu[2], Tina Geraki[4], Fred Mosselmans[4], Steve P. McGrath[2], Chris Grovenor[1] and Fang-Jie Zhao[5]

[1]Department of Materials, University of Oxford, Oxford, OX1 3PH, UK; [2]Rothamsted Research, Harpenden, Hertfordshire, AL5 2JQ, UK; [3]Department of Biological and Medical Sciences, Oxford Brookes University, Oxford, OX3 0BP, UK; [4]Diamond Light Source Ltd, Harwell Science and Innovation Campus, Chilton, Didcot, OX11 0DE, UK; [5]State Key Laboratory of Crop Genetics and Germplasm Enhancement, College of Resources and Environmental Sciences, Nanjing Agricultural University, Nanjing, 210095, China

Authors for correspondence:
Katie L. Moore
Tel: +44 (0)1865 273766
Email: katie.moore@materials.ox.ac.uk

Fang-Jie Zhao
Tel: +86 (0)2584396509
Email: fangjie.zhao@njau.edu.cn

Received: *9 June 2013*
Accepted: *12 August 2013*

New Phytologist (2014) **201:** 104–115
doi: 10.1111/nph.12497

Key words: arsenic, NanoSIMS, rice (*Oryza sativa*), synchrotron XRF, trace elements, vascular bundle.

Summary

- The cellular and subcellular distributions of trace elements can provide important clues to understanding how the elements are transported and stored in plant cells, but mapping their distributions is a challenging task.
- The distributions of arsenic, iron, zinc, manganese and copper, as well as physiologically related macro-elements, were mapped in the node, internode and leaf sheath of rice (*Oryza sativa*) using synchrotron X-ray fluorescence (S-XRF) and high-resolution secondary ion mass spectrometry (NanoSIMS).
- Although copper and silicon generally showed cell wall localization, arsenic, iron and zinc were strongly localized in the vacuoles of specific cell types. Arsenic was highly localized in the companion cell vacuoles of the phloem in all vascular bundles, showing a strong co-localization with sulfur, consistent with As(III)–thiol complexation. Within the node, zinc was localized in the vacuoles of the parenchyma cell bridge bordering the enlarged and diffuse vascular bundles, whereas iron and manganese were localized in the fundamental parenchyma cells, with iron being strongly co-localized with phosphorus in the vacuoles.
- The highly heterogeneous and contrasting distribution patterns of these elements imply different transport activities and/or storage capacities among different cell types. Sequestration of arsenic in companion cell vacuoles may explain the limited phloem mobility of arsenite.

Introduction

Plants require a number of micronutrients for their growth and development. Crops are an important source of essential trace elements for humans, but large numbers of the global population (> 2 billion) do not have adequate intakes of iron (Fe) and/or zinc (Zn) (WHO, 2002). Increasing the concentrations and/or bioavailability of these micronutrients in food crops can be an effective measure to alleviate micronutrient deficiencies in humans (White & Broadley, 2009). Plants also take up non-essential and toxic elements from the soil. Excessive accumulation of these toxic elements can affect plant growth and pose a risk to human health. One example is the accumulation of arsenic (As) by paddy rice, with rice consumption being the largest source to humans of carcinogenic inorganic As among food categories (Zhao *et al.*, 2010; Meharg & Zhao, 2012). Widespread contamination of soils with As in some rice-growing areas, for example, south and south-east Asia, further compromises agricultural sustainability and food safety (Meharg & Zhao, 2012). It is therefore important to understand how plants take up, transport, store and detoxify these elements. This also applies to essential micronutrients, which can become toxic when their accumulation in plant cells exceeds certain levels. For example, Fe toxicity is common in paddy rice because of the reductive nature of submerged paddy soils, resulting in the mobilization of Fe^{2+} (Becker & Asch, 2005), whereas manganese (Mn) toxicity can occur in crops growing on acidic and/or anaerobic soils (Marschner, 2012).

Plants contain *c.* 40 different cell types, often exhibiting different levels of element accumulation, although the role and mechanisms underlying the cell type-specific distributions of elements are still poorly understood (Conn & Gilliham, 2010). An important tool in plant nutrition research is the visualization of element distribution at different scales from the tissue, cellular to subcellular levels. This spatial information provides important clues to understanding the mechanisms of regulation of the homeostasis of essential and toxic minerals. Although numerous studies have investigated the cellular distributions of macronutrients or metals/metalloids in hyperaccumulator

plants, the visualization of trace elements in plant cells of non-hyperaccumulator species is much more challenging because of their low concentrations.

Recent technological advances have greatly enhanced the capability to spatially resolve trace elements in plant tissues and cells. A commonly used elemental mapping technique is synchrotron X-ray fluorescence (S-XRF) which, with modern detectors, has very good sensitivity for most elements. With the synchrotron, it is also possible to determine the speciation of elements of interest using X-ray absorption spectroscopy (XAS) techniques (Lombi *et al.*, 2011). A key disadvantage of S-XRF is the limited lateral or spatial resolution. On some beamlines, the beam size can be limited to *c.* 1 μm; however, even on beamlines on which the beam size can be focused to a few tens of nanometres, subcellular localization is still challenging because of the penetrating nature of the X-rays (and resulting fluorescence) (Lombi *et al.*, 2011). High-resolution secondary ion mass spectrometry (SIMS) or NanoSIMS uses an ion beam to bombard the surface of the material, which results in sputtering of the top few atomic layers; hence, it is very surface sensitive, unlike S-XRF, leading to excellent spatial resolution. The sputtered ions are analysed in a mass spectrometer, allowing chemical information to be obtained. NanoSIMS offers high spatial resolution (down to 50 nm) in combination with high elemental sensitivity (mg kg^{-1}), and can detect both the lighter elements as well as most of the heavier elements. The main disadvantage of NanoSIMS is that is has a limited field of view (50×50 μm^2 compared with many square millimetres for S-XRF), and analysis must be conducted in an ultra-high vacuum, meaning that complicated sample preparation protocols must be used in order to preserve the *in vivo* morphology and chemical distributions. A detailed description of the sample preparation required for SIMS can be found elsewhere (Moore *et al.*, 2012a), but the main point to be emphasized is that fast cryopreservation (usually under high pressure) and slow freeze substitution are necessary to preserve vacuolar contents. This sample preparation route does, however, prevent the analysis of the speciation of the elements, as resin embedding is known to cause changes in the speciation (Lombi *et al.*, 2009).

Although it is assumed that different trace elements will exhibit different cellular and subcellular distribution patterns in plant vascular tissues, little information is available on trace element distribution in crop species at high spatial resolution. The objective of this study was to map the cellular and subcellular distribution of As, Fe, Zn, Mn and copper (Cu) in the node, internode and leaf sheath of rice by combined use of S-XRF and NanoSIMS. This combination also allows us to probe the distribution of macro-elements that are physiologically related to the transport and homeostasis of trace elements. We focused on the node, internode and leaf sheath because they are the conducting tissues that are important for element transport in the shoot. The node, in particular, has complex and well-developed vascular bundles, and is a key controlling point determining the distribution of the elements between the vegetative and reproductive organs (Matsuo & Hoshikawa, 1993; Yamaji & Ma, 2009).

Materials and Methods

Plant growth

Rice (*Oryza sativa* L. cv Dongjin) plants were grown in hydroponic culture with half-strength Kimura nutrient solution in a controlled-environment glasshouse, as described in Zhao *et al.* (2012). At the beginning of flowering (65 d after germination), six plants were treated with 1.66 mM silicic acid and 10 μM sodium arsenite for 2 wk. The concentration of silicic acid used was higher than that expected in soil solution (typically 0.1–0.7 mM) (Savant *et al.*, 1997) to compensate for the short-term duration of the treatment, whereas the concentration of arsenite used was within the range found in the solutions of As-contaminated paddy soils (Khan *et al.*, 2010). Four replicates of plants were separated into the flag leaf blade, leaf sheath, the top node (node 1) and the internode 1. These were dried at 70°C for 48 h and digested with high-purity HNO_3/$HClO_4$. The concentrations of trace elements were determined using inductively coupled plasma-mass spectrometry (ICP-MS).

Sample preparation for spectroscopic analyses

A portion of the stems and leaf sheath were cut from the remaining replicates just above and below node 1 and quickly placed under MES buffer. A razor blade was then used to cut sections, *c.* 0.4–0.5 mm thick, and placed into a planchette coated with hexadecane. Another planchette was placed on top. Sections were frozen using a Bal-Tec HPM 010 high-pressure freezer (Bal-Tec/Leica, Wetzlar, Germany) with a pressure of 210 MPa at −196°C for 30 s. Freeze substitution was carried out in 1% glutaraldehyde in acetone as described previously (Moore *et al.*, 2011).

Samples for S-XRF were cut to a thickness of 10 μm using a Leica RM 2265 rotary microtome (Leica, Wetzlar, Germany). This thickness gave sufficient signal, but was not so thick that the S-XRF maps became distorted. Sections were then carefully placed into an envelope of Kapton tape.

After sectioning for S-XRF, samples were cut for NanoSIMS analysis using an RMC PowerTome ultramicrotome (Boeckeler Instruments Inc., Tucson, AZ, USA). It was decided not to use exactly the same section in the NanoSIMS as employed for S-XRF, as it was difficult to remove the section from the Kapton tape and to secure it flat to a NanoSIMS substrate, and the X-ray beam is quite damaging to the tissue (Moore *et al.*, 2010; Lombi *et al.*, 2011). As topography should always be avoided in SIMS analysis (Levi-Setti, 1988; Moore *et al.*, 2012b), it was decided to cut new sections of the appropriate thickness of 1 μm using a diamond knife and to place them onto platinum-coated plastic substrates as described previously (Moore *et al.*, 2011). The structures should not have changed considerably in the small distance between cutting the S-XRF and NanoSIMS sections, although some cells may have changed shape or have been completely lost because of their small size. To prevent charging during analysis, samples were coated with 5 nm of platinum just before loading into the NanoSIMS. Additional sections were cut for optical microscopy, placed onto glass slides and stained with toluidine blue.

S-XRF

S-XRF was undertaken at the Diamond Light Source on the microfocus beamline (I18) (Mosselmans *et al.*, 2009). The incident X-ray energy was set to 12.4 keV using an Si(111) monochromator. Samples in the Kapton tape envelopes were affixed to a plate attached to the sample stage. The sample was held at 45° to the incident X-ray beam and rastered in front of the beam whilst the X-ray fluorescence spectra were collected using a nine-element Ge detector positioned at 90° to the beam. The beam size was varied over the experiment to allow coarser, faster mapping (beam size, 20 μm) and finer scale mapping (beam size, 5 or 2 μm). Step sizes were matched to the beam size to avoid undersampling. As a result of the low bulk concentration of the elements of interest, the dwell time needed to be quite high: 0.5 s per pixel for most scans and 1 s per pixel for the beam size of 2 μm. As a result of time restrictions, only two replicates of the node and stem sections could be mapped. In calculations comparing the NanoSIMS and S-XRF data, the S-XRF counts were normalized by I_0, the incoming beam current. The fluorescence spectrum obtained from each pixel was fitted using the open-source software (PyMCA, Sole *et al.*, 2007) and elemental maps were created using these fitted data.

NanoSIMS

A NanoSIMS 50 instrument was used for high-resolution SIMS analysis. A 16-keV Cs^+ ion beam was scanned over the surface, generating negative secondary ions which were analysed using a double-focusing mass spectrometer. As a result of the low bulk concentrations of some of the elements of interest, it was important to carefully calibrate the position of the detectors on standards to ensure that the correct element was analysed and not a mass interference. The detectors for As, silicon (Si), phosphorus (P), MnO, Cu, ZnO and FeO were tuned on GaAs, an Si wafer, GaP, pure Mn, Cu and Zn and a steel sample, respectively. To ensure images from different samples were as comparable as possible and that the area was at steady state, Cs^+ ions were implanted into the sample to achieve a dose of 1×10^{17} ions cm^{-2}. Images were acquired with a dwell time of 60 ms at a size of 50×50 μm^2 and 256×256 pixels. NanoSIMS data were analysed using ImageJ with the OpenMIMS plugin (Harvard, Cambridge, MA, USA). The NanoSIMS counts from the whole image were normalized by the $^{12}C^{14}N^-$ signal to minimize differences in primary beam intensities when comparing with S-XRF data.

Results

Bulk tissue concentrations of trace elements

At the flowering stage and after exposure to arsenite and silicic acid for 2 wk, the rice node contained significantly higher concentrations of As, Fe, Zn and Cu than other tissues, for example, 22-, 19-, 16- and four-fold higher, respectively, than the concentrations in the internode (Fig. 1). Conversely, there was no strong accumulation of Mn in the node, the highest concentration being found in the leaf blade.

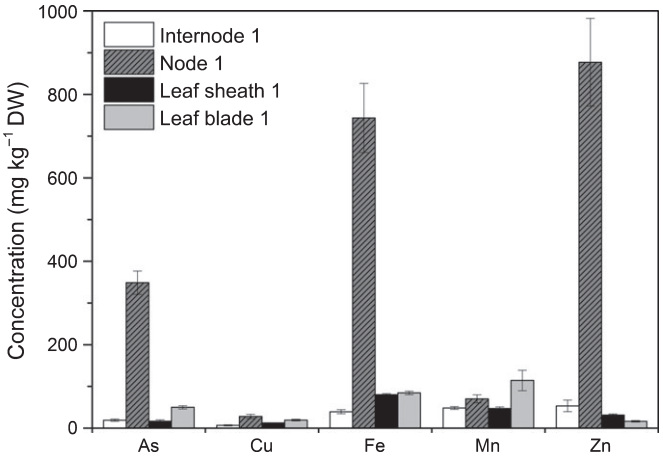

Fig. 1 The bulk tissue concentrations of arsenic (As), copper (Cu), iron (Fe), manganese (Mn) and zinc (Zn) in internode 1, node 1 (the top node), flag leaf sheath and leaf blade of rice (*Oryza sativa*), determined by inductively coupled plasma-mass spectrometry (ICP-MS). Error bars represent ± SE.

Element distributions in the internode

S-XRF maps acquired from the internode above node 1 show three large vascular bundles (LVBs) in the centre of the image and small vascular bundles (SVBs) on the right-hand side (Fig. 2a–g). On the left-hand side, there is a long band of vascular cells, likely to be a diffuse vascular bundle (DVB) extending from the node below. This section was cut from near the base of the internode and the structure is characteristic of this region (Matsuo & Hoshikawa, 1993). The centre of the internode (medullary cavity) is to the left and was not imaged. The morphology of the mapped region is shown in the optical image (Fig. 2a) and, to some extent, in the Zn map (Fig. 2e). An annotated high-resolution optical image of another section from this sample is shown in Supporting Information Fig. S1.

The five trace elements imaged showed distinct distribution patterns in the S-XRF maps (Fig. 2). There was strong accumulation of As in the LVBs, SVBs and DVBs, but only within the phloem region (Fig. 2f). Cu was located in similar regions in the three types of vascular bundles; however, in the merged images (Fig. 2g), Cu appeared to be strongly localized in an outer ring of cells outlining the phloem. The highest concentrations of Mn, Fe and Zn (Fig. 2b,c,e, respectively) were found in the fundamental parenchyma (FP) cells between and surrounding the LVBs. The FP cells form an open structure with many air spaces between the cells (Fig. S1). Although the distribution of the three elements in these FP cells looks similar in the individual element maps, the red, green, blue (RGB) colour merge image (Fig. S2) shows variations, with some cells containing all three elements, but others predominantly containing one or two. Although Fe appeared to be almost completely excluded from all types of vascular bundles, Zn and, to a lesser extent, Mn were localized within the vascular bundles but not the xylem vessels.

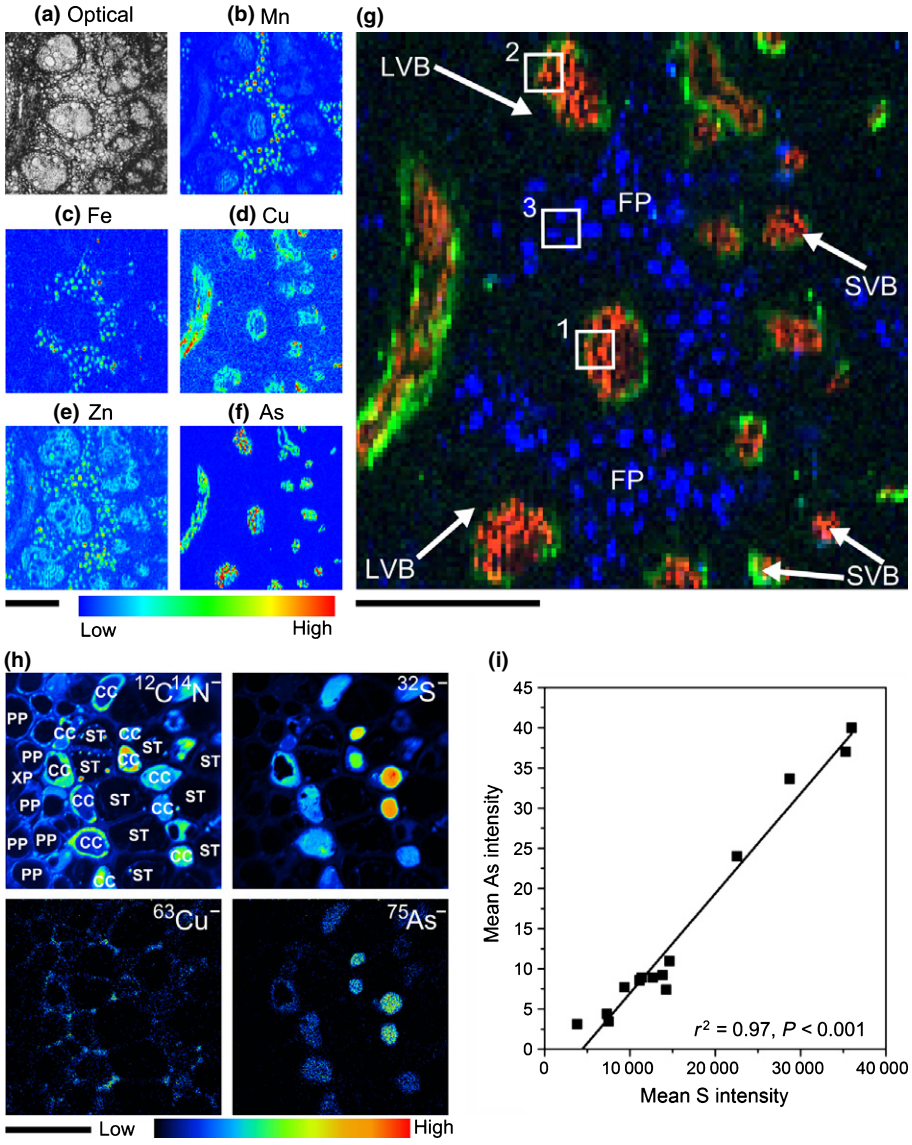

Fig. 2 Synchrotron X-ray fluorescence (S-XRF) and high-resolution secondary ion mass spectrometry (NanoSIMS) images of the internode above node 1 of rice (*Oryza sativa*); centre of internode is towards the left, epidermis to the right. (a) Optical image of the area mapped with S-XRF, (b) manganese (Mn), (c) iron (Fe), (d) copper (Cu), (e) zinc (Zn) and (f) arsenic (As). (g) Colour merge showing relative locations of As (red), Cu (green) and Fe (blue). (h) NanoSIMS images acquired from area 1 (box 1 in g) from an adjacent section. (i) Plot of mean sulfur (S) vs mean As intensity from the companion cells, showing strong correlation between these two elements. CC, companion cell; FP, fundamental parenchyma; LVB, large vascular bundle; PP, phloem parenchyma cell; ST, sieve tube; SVB, small vascular bundle; XP, xylem parenchyma cell. Bars: (a–g) 200 μm; (h) 20 μm. Areas 2 and 3 (boxes 2 and 3 in g) are shown in Supporting Information Figs S3 and S4, respectively.

NanoSIMS images (Figs 2h, S3) were acquired from an adjacent microtomed section to that imaged by S-XRF, and three analysed regions are marked by white squares on the RGB image (Fig. 2g) to show their positions relative to the S-XRF maps. The S-XRF maps were used to find regions of high element intensity so that NanoSIMS analysis could be precisely targeted to investigate their distributions at higher resolution. Both areas 1 and 2 were focused on the phloem region of the LVB, where the highest signals of As and Cu were found in the S-XRF maps. Ion maps were generated for $^{75}As^-$, $^{63}Cu^-$, as well as $^{12}C^{14}N^-$, $^{28}Si^-$ and $^{32}S^-$; the last three cannot be imaged by S-XRF because of the detector and conditions used in this experiment. The $^{28}Si^-$ image is not shown as almost no Si was found in the phloem regions. Comparison of the $^{12}C^{14}N^-$ and secondary electron (SE) images (Fig. S3) allows the individual cell types to be identified, for example, the metaxylem (MX) and xylem parenchyma (XP) cells with their characteristic thickened cell walls (Fig. 2h). XP cells have one thick cell wall and one thinner one; the latter is adjacent to the phloem parenchyma (PP) cells. Within the phloem, the sieve tubes (STs) and companion cells (CCs) are also identified (Figs 2h, S3); these exist in pairs, with the CCs located inside the STs towards the xylem side, with the STs being much larger and squarer (Matsuo & Hoshikawa, 1993). $^{75}As^-$ and $^{32}S^-$ signals were strongly localized in the CCs, but hardly detectable in the MX, XP, PP and ST cells. Furthermore, the high resolution of the NanoSIMS allowed the As and sulfur (S) signals to be localized in the vacuoles of CCs. The pairing of CCs and XP cells is particularly noticeable in Fig. 2(h), with two lines of cells containing high concentrations of As and S, separated by the STs, which did not contain S, Cu or As, and showed little cytoplasm, as indicated by the low signal of $^{12}C^{14}N^-$ relative to the CCs. This double line of As is in fact visible in the S-XRF image (Fig. 2g) but, with the higher resolution NanoSIMS images, it is now possible to accurately interpret the S-XRF data with regard to cell type. There was a very strong linear correlation ($r^2 = 0.97$, $P < 0.001$) between the intensity of As and S in regions of interest

(ROIs) within the vacuoles of the CCs (Fig. 2i); a similar strong correlation can be generated for all CCs analysed in the LVBs (Fig. 2) and SVBs (Fig. S4) in the internode region.

The higher resolution NanoSIMS images also make it possible to determine the localization of Cu in the phloem. In the S-XRF map, it would appear that Cu is co-localized with As in the CCs of the phloem, but the NanoSIMS images in Figs 2(h) and S5 show that it is in fact predominantly localized to the intercellular spaces surrounding the CCs and in the cell walls, with a low concentration in the CCs themselves. This Cu may be bound by pectins in the cell walls (Kopittke *et al.*, 2011). The S-XRF map shows Cu to be present in the phloem region of the LVBs, whereas the NanoSIMS image shows that the Cu signal only extends through the phloem as far as the PP cells.

The yield of $^{56}Fe^-$ in SIMS analysis is very low with the Cs^+ source, and so $^{56}Fe^{16}O^-$ was mapped instead to reveal the Fe distribution (Moore *et al.*, 2012c). Area 3 (marked in Fig. 2g), showing a high Fe signal in the S-XRF image, was mapped with NanoSIMS (Fig. 3). By comparing the $^{12}C^{14}N^-$ image with the position of localization of $^{56}Fe^{16}O^-$ at a subcellular scale, $^{56}Fe^{16}O^-$ was found to be strongly localized in the vacuoles of FP cells, with a more diffuse distribution throughout the rest of the cell, and no signal from the cell walls and starch grains. In this cell type, the vacuoles no longer fill the majority of the cell (as can be seen in the $^{12}C^{14}N^-$ image) and appear shrunken with irregular edges, as also observed in the light microscope image stained with toluidine blue (Fig. S1). $^{28}Si^-$ was localized in the cell walls of the FP. As expected from S-XRF mapping, very little As was found to be localized in this region, although the As signal was slightly elevated in the vacuoles.

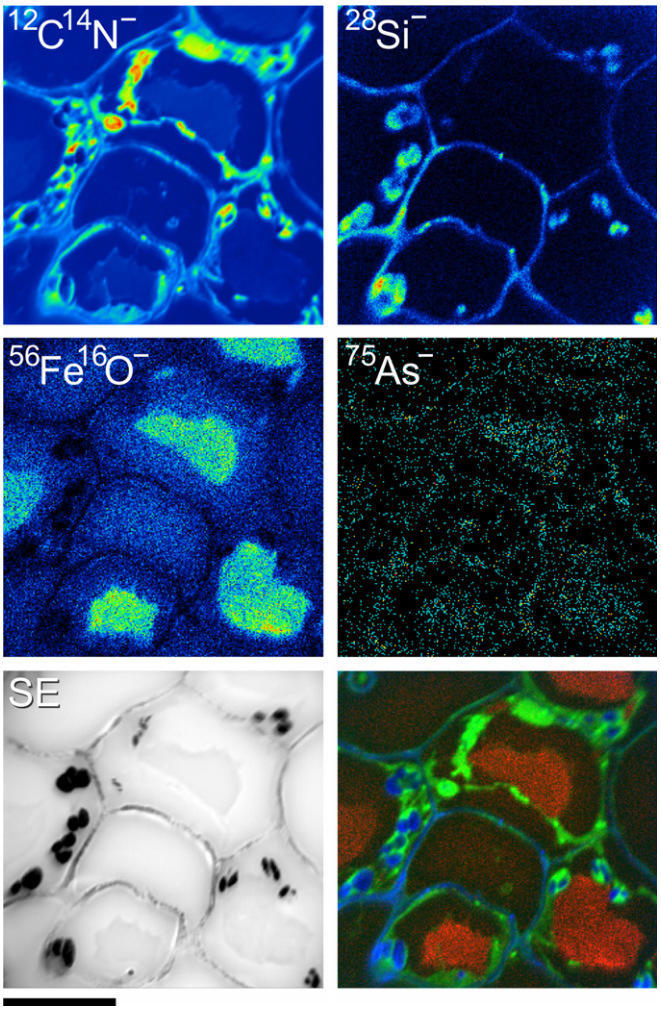

Fig. 3 High-resolution secondary ion mass spectrometry (NanoSIMS) images showing the distribution of $^{56}Fe^{16}O^-$ in the fundamental parenchyma of the internode of rice (*Oryza sativa*) taken from area 3 marked in Fig. 2(g). The image is summed from 12 sequential images. Colour merge shows $^{56}Fe^{16}O^-$ (red), $^{12}C^{14}N^-$ (green), $^{28}Si^-$ (blue). Dark features in the secondary electron (SE) image are starch grains. Bar, 15 μm.

Element distributions in the node

Figure 4(a–g) shows S-XRF maps from a section of node 1; an annotated image and the corresponding optical image showing the morphology of the cells can be seen in Fig. S6. Two enlarged vascular bundles (EVBs) can be seen filling most of the image; these have a distinctive keyhole shape and are almost completely devoid of any S-XRF signals, except in the phloem, where As (Fig. 4f) and Cu (Fig. 4d) are accumulated strongly. Within these EVBs, the phloem can be seen towards the top of the image and is shown most clearly in the As image in a heart shape. Surrounding each of the EVBs are the smaller DVBs, which show a strong accumulation of As and, to a lesser extent, Cu. Both elements were also localized inside the LVB, as observed towards the bottom of the image. All the different types of vascular bundle appeared to contain very little Mn, Zn or Fe. Fe and Mn were localized in the FP as observed in the internode; however, Mn was concentrated towards the middle of the node closest to the pithy centre and surrounding the LVBs, whereas Fe had a much more widespread distribution across the section and was also observed near the outside edge of the node section. Zn was strongly localized in XP cells bordering the EVBs and DVBs (Fig. 4e,g); these parenchyma cells are termed the parenchyma cell bridge (Yamaji & Ma, 2009). In contrast with the internode, very little Zn was present in FP cells, where Fe and Mn levels were elevated. It is striking from the S-XRF maps of the node and, especially, the RGB colour merge (Fig. 4g) that the As, Zn and Fe distributions are completely different. The only elements which seemed to co-localize were As and Cu, mainly in the DVBs, and Fe and Mn in the FP.

NanoSIMS images were acquired on an adjacent microtomed section from the white bordered areas in Fig. 4(g). Area 1 was acquired from one of the DVBs (Fig. 4h) and there is very good agreement between the distribution of As as mapped by S-XRF and NanoSIMS. The S-XRF map suggests some variation in the As distribution within the DVB, but only with NanoSIMS is it possible to determine that only some of the cells in this region in fact contain high concentrations of As. Again S and As are co-localized in the DVB in the vacuoles of the CCs within the enlarged phloem, whereas the two elements are barely detectable in the STs. As with the internode, there is a strong linear correlation between As and S ($r^2 > 0.65$, $P < 0.001$) for all DVBs analysed. Very little Si is present across the phloem of the DVB, but

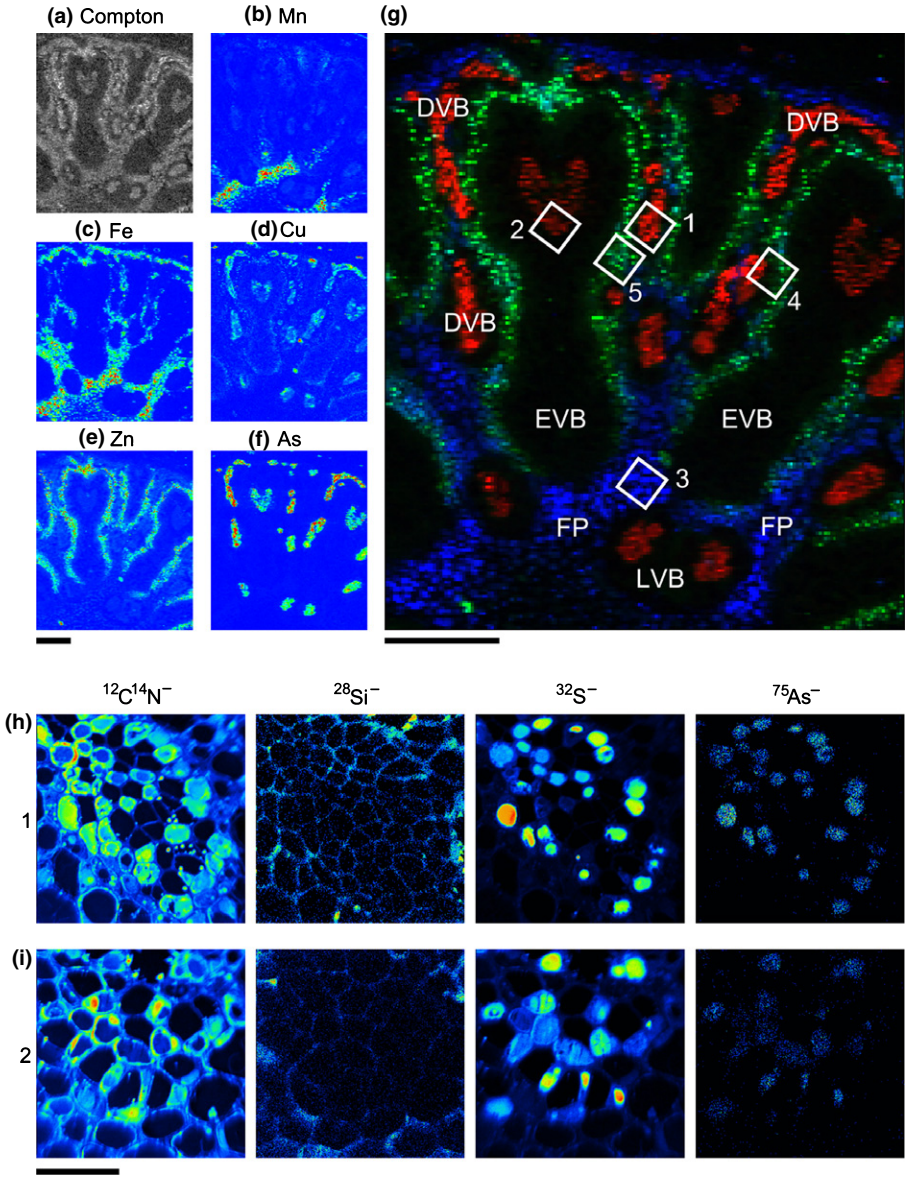

Fig. 4 Synchrotron X-ray fluorescence (S-XRF) and high-resolution secondary ion mass spectrometry (NanoSIMS) images of a section of node 1 of rice (*Oryza sativa*). (a) Compton scattering image of area mapped with S-XRF, (b) manganese (Mn), (c) iron (Fe), (d) copper (Cu), (e) zinc (Zn) and (f) arsenic (As). (g) Colour merge showing the relative locations of As (red), Zn (green) and Fe (blue). (h) NanoSIMS images acquired from the phloem region of a diffuse vascular bundle (area 1 on g). (i) NanoSIMS images acquired from the phloem of the enlarged vascular bundle (area 2 on g). The NanoSIMS images have been rotated *c.* 40° anticlockwise from the white boxes marked in (g), and the NanoSIMS Si image of (h) is presented on a logarithmic scale for clarity. DVB, diffuse vascular bundle; EVB, enlarged vascular bundle; FP, fundamental parenchyma; LVB, large vascular bundle. Bars: (a–g) 200 μm; (h, i) 20 μm. Areas 3–5 are presented in Figs 6 and 7, respectively.

cell walls surrounding the phloem contain a higher concentration. Figure 4(i) shows NanoSIMS images from a phloem region of the EVB (area 2). In contrast with the internode, the pairing of the CCs and STs is not as clear in the EVB; instead, the cells in the phloem appear to be distributed quite randomly, as are the PP cells (Matsuo & Hoshikawa, 1993). Again, there is strong co-localization of As with S in the CCs ($r^2 = 0.91$, $P < 0.001$).

One region of the section showed the presence of a lateral DVB in addition to the normal vertical DVBs (Fig. 5a). This lateral DVB appears to connect three DVBs which run parallel to the EVB. The morphology of the cells in the lateral DVB is very similar to that in the vertical DVBs, with CCs and STs (which appear empty), except that the cells have been sectioned longitudinally in this case. As with all the DVBs around the EVB, the CCs in the lateral DVB show high concentrations of S and As (Fig. 5b,c); however, there is also a distinct increase in the concentration of Cu within the CCs. The difference in Cu intensity is clearly visible in Fig. 5(c), where a vertical DVB has been imaged alongside the lateral DVB. Figure 5(d) shows linear correlations between the S and Cu intensities and between the S and As intensities in the CCs of the lateral DVB imaged in Fig. 5(b), but the correlations are not as statistically significant compared with the phloem regions of other vascular bundles mapped in the node and internode (see Fig. S4, where $P < 0.001$).

In Fig. 5(c), where two different types of DVB have been mapped in one image, the correlation plots (Fig. 5e) show the effect of Cu in the cells on the amount of As which can be complexed by S. Within the vertical DVB, there is very strong correlation between the S and As intensities and a much weaker correlation between S and Cu. The intensity of As within the lateral DVB is much reduced from that which would be expected based on the intensity of S and the trend line fitted to the DVB data. Concurrently, there is a significantly higher intensity of Cu in these three cells of the lateral DVB (circled). This suggests that there is competition between Cu and As for the S-containing ligands in the lateral DVB.

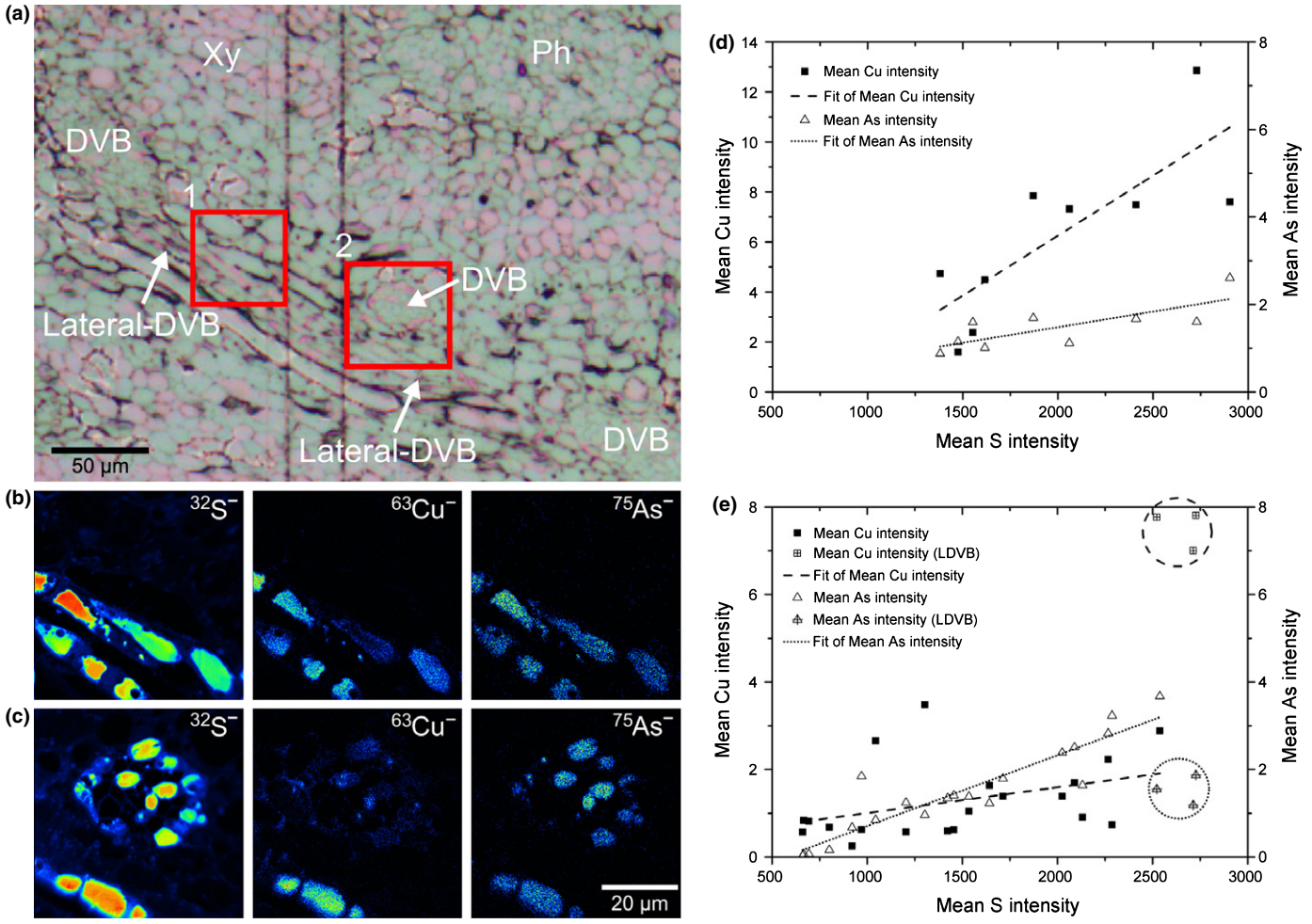

Fig. 5 High-resolution secondary ion mass spectrometry (NanoSIMS) images of a lateral diffuse vascular bundle (DVB) in node 1 of rice (*Oryza sativa*). (a) Optical micrograph of the section analysed with NanoSIMS. Areas in which NanoSIMS analysis was undertaken are marked 1 and 2 corresponding to the NanoSIMS images in (b) and (c), respectively. (b) and (c) show $^{32}S^-$, $^{63}Cu^-$ and $^{75}As^-$ NanoSIMS maps. In (b), part of the lateral DVB and part of the parenchyma cell bridge were mapped, whereas, in (c), part of the lateral DVB and a whole cross-section of a DVB were mapped. The graphs of (d) and (e) are correlation plots of $^{32}S^-$ intensity vs $^{63}Cu^-$ and $^{75}As^-$ intensity, (d) relates to (b), whereas (e) relates to (c). In (e), the symbols with a + through the centre and highlighted in a ring correspond to the signals from the three lateral DVB cells at the bottom of (c). r^2 values for (d) are 0.59 ($P < 0.016$) for As and 0.63 ($P < 0.011$) for Cu. For (e), they are 0.79 ($P < 0.001$) for As and 0.13 ($P < 0.001$) for Cu (excluding the three lateral DVB cells). Ph, phloem; Xy, xylem.

Fe was found to be strongly accumulated in the node region, as shown by ICP-MS and S-XRF analysis. Figure 6(a), acquired by NanoSIMS analysis from area 3 in Fig. 4(g), shows strong Fe accumulation in the vacuoles of the FP, similar to that observed in the internode. However, there are a number of structural differences. Here, the vacuoles are not shrunken and each cell appears to contain several vacuoles. Although the $^{56}Fe^{16}O^-$: $^{31}P^-$ ratio within an individual cell is almost the same for each vacuole, Fig. 6(a) shows large differences in the $^{56}Fe^{16}O^-$ signal between cell vacuoles, varying by up to a factor of five. Similar large variations in the Fe signal were also observed in the S-XRF map. $^{56}Fe^{16}O^-$ was found to correlate very strongly with $^{31}P^-$ in all FP cell vacuoles (Fig. 6b).

Both S-XRF and NanoSIMS provide semi-quantitative data, which can be made quantitative by the use of appropriate standards; however, NanoSIMS is prone to matrix effects which can make precise quantification difficult. Thus, it is reassuring to observe that the ratio of the Fe counts between the node and internode, 18.4 and 11 for S-XRF and NanoSIMS measurements, respectively, is similar to the same ratio in the ICP-MS data (19, Fig. 1). The reasonable agreement between the three methods provides a validation for the comparison of the NanoSIMS or S-XRF signal intensity between cell types.

Mapping of $^{64}Zn^{16}O^-$ (for Zn) and $^{55}Mn^{16}O^-$ (for Mn) was also attempted in NanoSIMS. Mapping of $^{55}Mn^{16}O^-$ was unsuccessful, as the local concentration was below the detection limit, but it was possible to produce maps of $^{64}Zn^{16}O^-$ from the node where the concentration was significantly higher than in the internode. Figure 7(a) shows where the Zn is localized in the parenchyma cell bridge and in relation to the DVB. Part of a DVB can be seen in the bottom left of Fig. 7(a), as clearly indicated by the characteristic distribution of As in the CCs. Moving towards the top right of the image, the next layer is the xylem transfer cells shown in the $^{12}C^{14}N^-$ image by the lack of

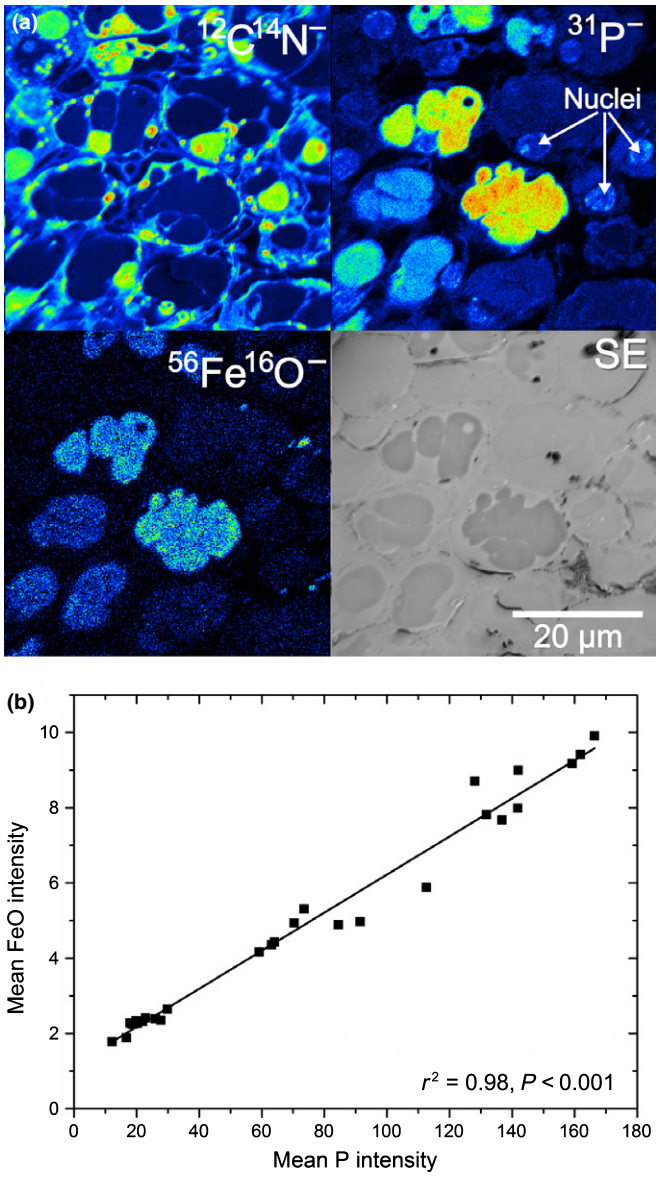

Fig. 6 (a) High-resolution secondary ion mass spectrometry (NanoSIMS) images showing the distribution of $^{56}Fe^{16}O^-$ in the fundamental parenchyma of the node of rice (*Oryza sativa*) taken from area 3 in Fig. 4(g) (image not summed from sequential images). (b) Graph showing the strong correlation between $^{31}P^-$ and $^{56}Fe^{16}O^-$ in the fundamental parenchyma vacuoles. SE, secondary electron image.

$^{12}C^{14}N^-$ signal inside the cells. In the top right of the image, XP cells can be observed, and it is these which contain the high concentrations of Zn that are observed by S-XRF. Figure 7(b) shows the $^{64}Zn^{16}O^-$ and $^{56}Fe^{16}O^-$ distributions from a slightly thicker region of parenchyma cells around an EVB. In both regions, $^{64}Zn^{16}O^-$ is localized in the vacuoles of the parenchyma cells. Some of the vacuoles contain significantly larger amounts of Zn than others, which is consistent with the variations seen in the S-XRF maps. The $^{12}C^{14}N^-$ images of these cells showed the presence of multiple, variously sized vacuoles within each cell, which may explain the spotty appearance of the Zn signal in the S-XRF map. Fe is only slightly more enriched in the vacuoles which contain $^{64}Zn^{16}O^-$ than in the surrounding cells, but some $^{56}Fe^{16}O^-$ was expected in this region based on the S-XRF mapping. In Fig. 7(a,b), many plasmodesmata can be observed, a few of which have been marked with white arrows.

Element distributions in the leaf sheath

In a separate synchrotron experiment (but using the same analysis conditions), part of the base of the leaf sheath was also mapped. In this case, the NanoSIMS sections were not taken from the same specimen as that mapped by the synchrotron, but were from the same plant. The S-XRF image (Fig. 8b) shows that, across the width of the leaf sheath, As was only found to be localized within the phloem region of the LVBs, and this was also where Cu and Fe were localized. Zn was found to be localized mainly within the vascular bundle but, contrary to the node and internode, was not localized around the vascular bundles, presumably because of the absence of vacuoles in this part of the plant. A higher concentration of Zn and Mn was observed in a similar location to As (data not shown). Higher resolution S-XRF images (Fig. 8c–e) of this phloem region indicate that As is only localized in a band of cells close to the xylem vessels, and Fe appears to be localized around the edge of the phloem. This Fe distribution was not observed around the phloem in either internode or node, where Fe appeared to be excluded from the vascular bundles. NanoSIMS imaging (Fig. 8f) revealed an almost identical distribution of As to S-XRF, with the vacuoles of the CC cells near the side of the xylem vessels containing the most As and those further away from the xylem containing significantly less. As with the node and internode, there is a strong co-localization of As with S in the vacuoles of the CCs, with the counts of the two elements correlating significantly ($r^2 = 0.85$, $P < 0.001$, see Fig. S4).

Discussion

Combining NanoSIMS and S-XRF mapping has proven to be a powerful methodology to determine the previously unknown distribution patterns of trace elements in rice tissues. This combination has the following key advantages: elemental mapping with sufficient resolution to probe subcellular and cellular distributions; high sensitivity which is required for trace elements with bulk tissue concentrations in the mg kg^{-1} range; and the ability to detect a wide range from lighter (S, P, Si) to heavier (As, Cu, Fe, Zn) elements. This greatly aids the physiological interpretation of the data obtained.

For both techniques, especially NanoSIMS, sample preparation is of vital importance. Previous studies have shown that the method of high-pressure freezing, followed by freeze substitution, preserves the *in vivo* localization of mobile elements (Smart *et al.*, 2010; Moore *et al.*, 2011). This is further confirmed by the present study, where distinct distribution patterns of different trace elements and the strong localization of some elements in vacuoles indicate that element redistribution has not occurred during sample preparation. With S-XRF, the X-ray beam can be quite damaging to the specimen (Lombi *et al.*, 2011), making analysis of

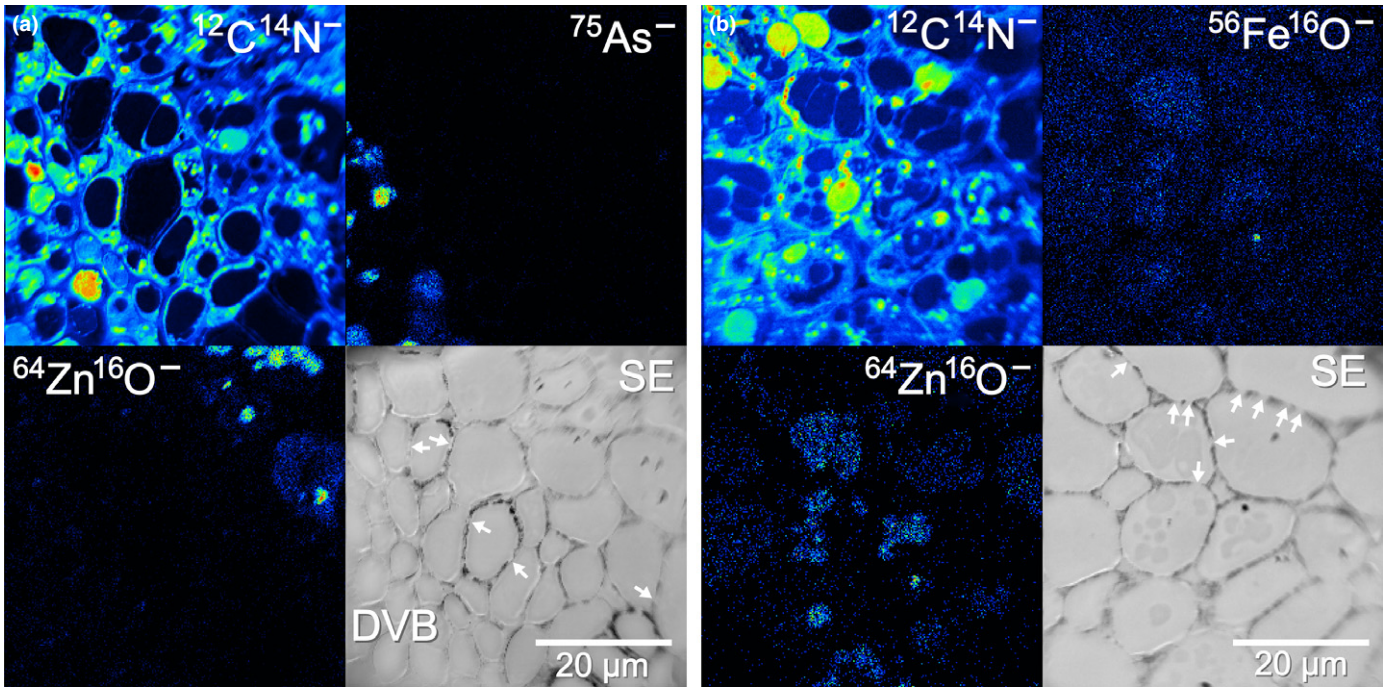

Fig. 7 (a) High-resolution secondary ion mass spectrometry (NanoSIMS) images from the parenchyma cell bridge of the node of rice (*Oryza sativa*) showing where $^{64}Zn^{16}O^-$ is localized relative to the diffuse vascular bundle (area 4 in Fig. 4g). (b) NanoSIMS images showing that $^{64}Zn^{16}O^-$ is accumulated in the vacuoles of the parenchyma cells with hotspots found in some of the cells, consistent with that observed by synchrotron X-ray fluorescence (S-XRF) (area 5 in Fig. 4g). DVB, diffuse vascular bundle; SE, secondary electron image. Arrows indicate plasmodesmata.

the same specimen with both techniques difficult. This problem was resolved in our study by using adjacent thin sections of the same sample. A remarkable similarity in the distribution of the elements was observed between the two techniques, which allowed the distributions to be investigated from the millimetre to the subcellular scale.

A novel and striking observation from the present study is that As is strongly localized in the vacuoles of the CCs within the phloem in different types of vascular bundles, where the intensity of the As signal is *c.* 150–300 times higher than that in the surrounding cells. This localization pattern also explains why the As concentration is much higher in the node than in the internode and leaf tissues, because the node contains proportionally more vascular bundles responsible for the distribution of nutrients (and toxic elements) and photosynthates between leaves and the panicle (Yamaji & Ma, 2009). We have estimated that, in the node section, the As concentration in the CCs can be as high as 8400 mg kg^{-1} DW. We determined the ratio of As counts detected in the CCs compared with other cells (ST, PP, XP, etc.) and adjusted the bulk concentration by this ratio to determine what fraction of the total As was localized in the CCs. This value was then divided by the fraction of the node estimated to be CCs to give the As concentration in the CCs. Based on the criterion commonly used to define As hyperaccumulators, > 1000 mg kg^{-1} in the bulk above-ground tissue (Ma *et al.*, 2001), rice is not an As hyperaccumulator, but the CCs in the vascular bundles in the node and internode can be considered to be As hyperaccumulating cells. The above calculations serve to highlight two important points: first, bulk tissue concentrations can be misleading because the cellular As distribution is extremely heterogeneous, and, second, strong As detoxification must be in operation in the CCs.

Our previous study also showed strong co-localization of As and S in the vacuoles in the pericycle and endodermal cells of rice roots (Moore *et al.*, 2011). Based on the strong co-localization of As and S in the vacuoles of the CCs in the results presented here, As is most probably detoxified by complexation with thiol-containing ligands, such as phytochelatins (PCs), with the As–thiol complexes subsequently being sequestered in the vacuoles (Liu *et al.*, 2010; Song *et al.*, 2010). The role of PCs in As detoxification in non-hyperaccumulator plants has been well established. The *Arabidopsis thaliana* mutants defective in PC synthesis are highly sensitive to As (Ha *et al.*, 1999; Liu *et al.*, 2010). A number of arsenite–PC complexes have been identified in plants (Raab *et al.*, 2005; Liu *et al.*, 2010). The ABCC-type vacuolar transporters responsible for the tonoplast transport of arsenite–PC complexes have also been identified in *Arabidopsis* (Song *et al.*, 2010). The S : As ratio in the CC vacuoles from the NanoSIMS data (taking into account the relative sensitivity factors of these two elements) was always > 3 : 1 (this being the expected molar ratio for the thiol group : arsenite). This suggests that the CCs had produced more thiol than required to complex all the As, and that the plant was not suffering from As toxicity (which was not observed in the experiment). To be able to produce large concentrations of thiol compounds, the CCs must also have a more enhanced S metabolism than other surrounding cell types. The strong sequestration of As–thiol compounds in the CC vacuoles is likely to restrict the movement of As into the STs of the phloem, thus explaining why As is relatively immobile in the

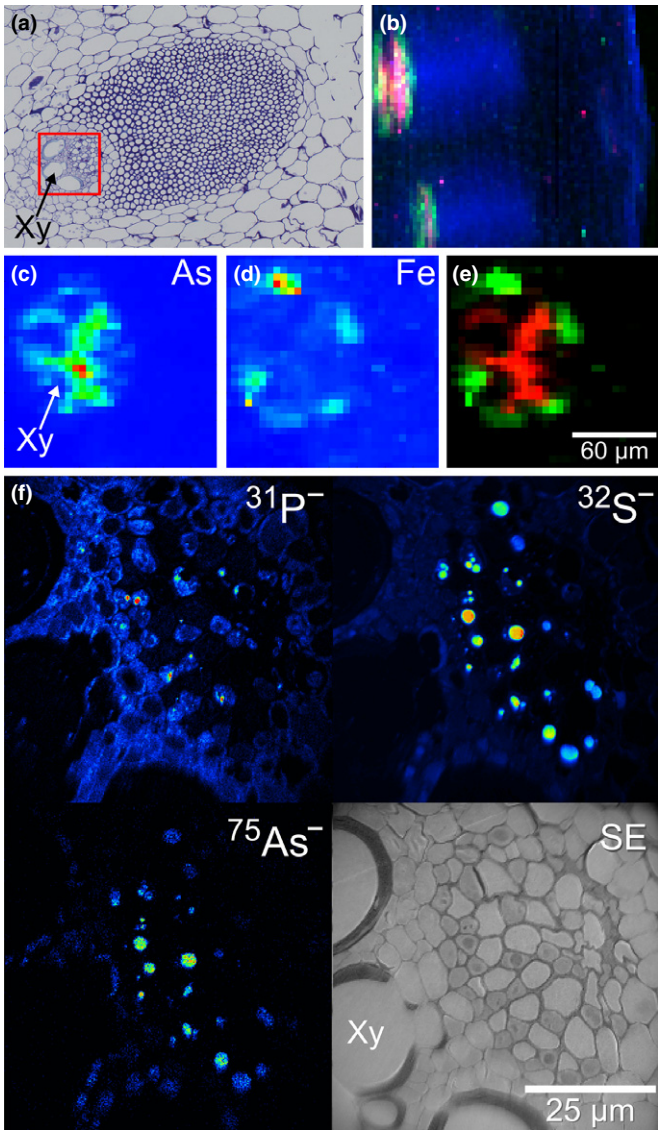

Fig. 8 Synchrotron X-ray fluorescence (S-XRF) and high-resolution secondary ion mass spectrometry (NanoSIMS) images of one of the vascular bundles from the leaf sheath of rice (*Oryza sativa*). (a) Stained optical image of a vascular bundle, (b) low-resolution S-XRF image showing two large vascular bundles (LVB) and the outside of the leaf sheath on the right; arsenic (As), red; iron (Fe), green; zinc (Zn), blue. High-resolution S-XRF images of (c) As and (d) Fe from the phloem region of the LVB (red square in a); (e) colour merge image showing the relative locations of (c) (As, red) and (d) (Fe, green). (f) NanoSIMS images showing the subcellular localization of $^{31}P^-$, $^{32}S^-$ and $^{75}As^-$ in the phloem region near the xylem (Xy) vessels. Note the very similar distribution of As observed in the NanoSIMS and S-XRF images. SE, secondary electron image.

long-distance transport to the rice grain; however, a small amount of As does reach the grain, and this transport has been shown to be mainly via the phloem (Carey *et al.*, 2010; Zhao *et al.*, 2012), which is also supported by the As localization pattern revealed in the present study.

A question arises as to why As is so specifically stored in the vacuoles of the CCs. This may result from one or more of the following: CCs may have a strong ability to transport As across the plasma membranes into the cells; the capacity to synthesize PCs is greatly enhanced in the CCs; and the ABCC-type arsenite–PC transporters may be highly expressed in the tonoplast of the CCs. To address this question, further studies are needed to investigate gene expression patterns in individual cell types.

Although it has been shown that arsenite and silicic acid share the same uptake pathway in rice roots (Ma *et al.*, 2008), Si has a markedly different distribution pattern from that of As in the node and internode. Si is localized in the cell walls of the FP (Fig. 3), the parenchyma cell bridge (Fig. S7) and, to some extent, in the cell walls of the phloem of the DVBs and EVBs (Fig. 4h,i). This is not unexpected as most of the Si transported to the rice shoots is deposited in the apoplast of leaves and husk, especially in the specific Si cells (Ma & Yamaji, 2006), rather than being deposited in the stems. Unlike As, Si is not complexed with PCs, and no Si is detected in the vacuoles, probably because of the lack of Si transporters located in the tonoplast. Surprisingly, Si was found to accumulate in oval granules, likely to be the starch grains, in the cytoplasm of the FP of the internode (Fig. 3). The biological significance of this accumulation is not known.

The transition metals Fe and Mn are strongly localized in FP cells in both the node and internode. NanoSIMS imaging further shows that Fe is stored in the vacuoles in these cells and is strongly co-localized with P, possibly as insoluble Fe–phosphate complexes. This observation is consistent with previous reports that P decreases Fe solubility and availability in rice plants (Zheng *et al.*, 2009). Similarly, using transmission electron microscopy (TEM) and energy-dispersive X-ray spectroscopy (EDX) analysis of chemically fixed specimens, Hirsch *et al.* (2006) showed the presence of Fe in the vacuoles of the cells surrounding the vasculature of *Arabidopsis* leaves as globular deposits with phosphate (Hirsch *et al.*, 2006). Vacuolar storage of Fe may be a way to sequester excess free Fe, which can cause oxidative stress (Morrissey & Guerinot, 2009). Strong co-localization of Fe and P in the vacuoles of FP cells may be an important mechanism employed by rice to detoxify Fe, as rice plants have to cope with greatly increased availability of Fe^{2+} in submerged paddy soil. The formation of insoluble Fe–P complexes in the vacuoles also explains the relatively low mobility of Fe in plants (Marschner, 2012). Mn, like Fe, is likely to be stored in the vacuoles in FP cells. Apart from this similarity, there are differences between Mn and Fe in their cellular distribution patterns. Fe also accumulates to some extent in the vacuoles of XP cells bordering the EVBs and DVBs, whereas Mn is found in the epidermal cells of the node (Fig. S8). At the tissue level, there is a large elevation of the concentrations of Fe, Zn and Cu, but not Mn, in the node compared with other tissues.

Similar to the recent report by Yamaguchi *et al.* (2012), Zn was found by S-XRF imaging to be localized strongly to XP cells in the node; these cells were named the parenchyma cell bridge by Yamaji & Ma (2009). For the first time in biological studies, NanoSIMS was used successfully to map the subcellular localization of Zn, an element with a very poor ionization yield. In these XP cells, Zn is stored in the vacuoles, as is Fe. These cells occupy an important position bordering the EVBs and DVBs, possibly controlling the transfer of Zn (and, to a lesser extent, Fe) from

the EVBs to DVBs; the latter deliver nutrients and photosynthates to the panicle. The form of Zn in the vacuoles is unknown in the present study. Possible ligands for complexation of Zn include organic acids, NA (nicotianamine), phosphate or phytates (Rauser, 1999; Salt *et al.*, 1999; Kopittke *et al.*, 2011).

Cu shows a very different distribution pattern from that of the other transition metals studied, with a strong localization to various types of vascular bundles. In fact, the distribution of Cu in certain cells is more similar to that of As, which may be related to the high affinity of both elements to thiol compounds. Cu is known to be complexed by metallothioneins (Cobbett & Goldsbrough, 2002) and there is evidence from extended X-ray absorption fine structure (EXAFS) analysis that Cu is bound to S ligands (Mijovilovich *et al.*, 2009; Ryan *et al.*, 2013). In the present study, Cu was found to be associated with S mainly in the vacuoles of the lateral DVBs in the node, but also in isolated CCs in the DVBs. It appears to be present mainly in the cell walls in other vascular bundles, but its localization only extends as far as PP cells (Figs 2, S5). Strong binding of Cu with polygalacturonic acid in cell walls has been observed in the rhizodermis and outer cortex of cowpea roots (Kopittke *et al.*, 2011).

By combining S-XRF and NanoSIMS, this study has shown distinctive cell type-specific distribution patterns of four essential and one toxic trace element, as well as physiologically related macro-elements, such as P, S and Si, in rice conducting tissues at both the cellular and subcellular scale. Vacuolar storage appears to be a common feature responsible for the strong localization in specific cell types, although Cu and Si are localized in some cell walls. Strong co-localization of As with S and Fe with P in specific cells also provides important clues to the detoxification mechanisms. The spatial distribution patterns of these elements are highly heterogeneous, implying different storage capacities and/or different functions in trace element homeostasis among different cell types. The distribution patterns observed should aid future research into the investigation of cell type-specific expression patterns of responsible genes (Conn & Gilliham, 2010). The combined imaging techniques can also be used to compare mutants or knockout/knockdown lines with wild-type plants to gain vital information with regard to gene functions. This information is essential for an understanding of how different trace elements are transported, stored, detoxified and distributed between the vegetative tissues and the grain.

Acknowledgements

K.L.M. is supported by Engineering and Physical Sciences Research Council (EPSRC) grant EP/I026584/1, F-J. Z., Y.C. and S.P.M. by Biotechnology and Biological Sciences Research Council (BBSRC) grant BB/H006303/1, and F-J.Z. by the National Natural Science Foundation of China (31372123) and the Innovative Research Team Development Plan (IRT1256) of the Ministry of Education of China. We thank Professor J. F. Ma and Dr N. Yamaji for advice on rice node structure, and Professor C. Hawes for help and advice with high-pressure freezing. We thank the Diamond Light Source for the provision of synchrotron beamtime under awards SP6042 and SP7087.

References

Becker M, Asch F. 2005. Iron toxicity in rice—conditions and management concepts. *Journal of Plant Nutrition and Soil Science* **168**: 558–573.

Carey AM, Scheckel KG, Lombi E, Newville M, Choi Y, Norton GJ, Charnock JM, Feldmann J, Price AH, Meharg AA. 2010. Grain unloading of arsenic species in rice. *Plant Physiology* **152**: 309–319.

Cobbett C, Goldsbrough P. 2002. Phytochelatins and metallothioneins: roles in heavy metal detoxification and homeostasis. *Annual Review of Plant Biology* **53**: 159–182.

Conn S, Gilliham M. 2010. Comparative physiology of elemental distributions in plants. *Annals of Botany* **105**: 1081–1102.

Ha SB, Smith AP, Howden R, Dietrich WM, Bugg S, O'Connell MJ, Goldsbrough PB, Cobbett CS. 1999. Phytochelatin synthase genes from Arabidopsis and the yeast *Schizosaccharomyces pombe*. *Plant Cell* **11**: 1153–1163.

Hirsch J, Marin E, Floriani M, Chiarenza S, Richaud P, Nussaume L, Thibaud MC. 2006. Phosphate deficiency promotes modification of iron distribution in Arabidopsis plants. *Biochimie* **88**: 1767–1771.

Khan MA, Stroud JL, Zhu YG, McGrath SP, Zhao FJ. 2010. Arsenic bioavailability to rice is elevated in Bangladeshi paddy soils. *Environmental Science & Technology* **44**: 8515–8521.

Kopittke PM, Menzies NW, de Jonge MD, McKenna BA, Donner E, Webb RI, Paterson DJ, Howard DL, Ryan CG, Glover CJ *et al.* 2011. *In situ* distribution and speciation of toxic copper, nickel, and zinc in hydrated roots of cowpea. *Plant Physiology* **156**: 663–673.

Levi-Setti RR. 1988. Structural and microanalytical imaging of biological materials by scanning microscopy with heavy-ion probes. *Annual Review of Biophysics and Biophysical Chemistry* **17**: 325–347.

Liu WJ, Wood BA, Raab A, McGrath SP, Zhao FJ, Feldmann J. 2010. Complexation of arsenite with phytochelatins reduces arsenite efflux and translocation from roots to shoots in Arabidopsis. *Plant Physiology* **152**: 2211–2221.

Lombi E, Scheckel KG, Kempson IM. 2011. *In situ* analysis of metal(loid)s in plants: state of the art and artefacts. *Environmental and Experimental Botany* **72**: 3–17.

Lombi E, Scheckel KG, Pallon J, Carey AM, Zhu YG, Meharg AA. 2009. Speciation and distribution of arsenic and localization of nutrients in rice grains. *New Phytologist* **184**: 193–201.

Ma LQ, Komar KM, Tu C, Zhang WH, Cai Y, Kennelley ED. 2001. A fern that hyperaccumulates arsenic. *Nature* **409**: 579.

Ma JF, Yamaji N. 2006. Silicon uptake and accumulation in higher plants. *Trends in Plant Science* **11**: 392–397.

Ma JF, Yamaji N, Mitani N, Xu X-Y, Su Y-H, McGrath SP, Zhao FJ. 2008. Transporters of arsenite in rice and their role in arsenic accumulation in rice grain. *Proceedings of the National Academy of Sciences, USA* **105**: 9931–9935.

Marschner P. 2012. *Marschner's mineral nutrition of higher plants*. London, UK: Academic Press.

Matsuo TE, Hoshikawa KE. 1993. *Science of the rice plant. Vol 1, Morphology*. Tokyo, Japan: Food and Agriculture Policy Research Center.

Meharg AA, Zhao FJ. 2012. *Arsenic & rice*. Dordrecht, the Netherlands: Springer.

Mijovilovich A, Leitenmaier B, Meyer-Klaucke W, Kroneck PMH, Gotz B, Kupper H. 2009. Complexation and toxicity of copper in higher plants. II. Different mechanisms for copper versus cadmium detoxification in the copper-sensitive cadmium/zinc hyperaccumulator *Thlaspi caerulescens* (Ganges ecotype). *Plant Physiology* **151**: 715–731.

Moore KL, Lombi E, Zhao FJ, Grovenor CRM. 2012a. Elemental imaging at the nanoscale: NanoSIMS and complementary techniques for element localisation in plants. *Analytical and Bioanalytical Chemistry* **402**: 3263–3273.

Moore KL, Schröder M, Grovenor CRM. 2012b. Imaging secondary ion mass spectrometry. In: Tendeloo GV, Van Dyck D, Pennycook SJ, eds. *Handbook of nanoscopy*. Weinheim, Germany: Wiley-VCH, 709–744.

Moore KL, Schroder M, Lombi E, Zhao FJ, McGrath SP, Hawkesford MJ, Shewry PR, Grovenor CRM. 2010. NanoSIMS analysis of arsenic and selenium in cereal grain. *New Phytologist* **185**: 434–445.

Moore KL, Schroder M, Wu Z, Martin B, Hawes C, McGrath SP, Hawkesford MJ, Ma JF, Zhao FJ, Grovenor CRM. 2011. High resolution secondary ion mass spectrometry reveals the contrasting subcellular distribution of arsenic and silicon in rice roots. *Plant Physiology* **156**: 913–924.

Moore KL, Zhao F-J, Gritsch CS, Tosi P, Hawkesford MJ, McGrath SP, Shewry PR, Grovenor CRM. 2012c. Localisation of iron in wheat grain using high resolution secondary ion mass spectrometry. *Journal of Cereal Science* **55**: 183–187.

Morrissey J, Guerinot ML. 2009. Iron uptake and transport in plants: the good, the bad, and the ionome. *Chemical Reviews* **109**: 4553–4567.

Mosselmans JFW, Quinn PD, Dent AJ, Cavill SA, Moreno SD, Peach A, Leicester PJ, Keylock SJ, Gregory SR, Atkinson KD *et al.* 2009. I18—the microfocus spectroscopy beamline at the Diamond Light Source. *Journal of Synchrotron Radiation* **16**: 818–824.

Raab A, Schat H, Meharg AA, Feldmann J. 2005. Uptake, translocation and transformation of arsenate and arsenite in sunflower (*Helianthus annuus*): formation of arsenic–phytochelatin complexes during exposure to high arsenic concentrations. *New Phytologist* **168**: 551–558.

Rauser WE. 1999. Structure and function of metal chelators produced by plants – the case for organic acids, amino acids, phytin, and metallothioneins. *Cell Biochemistry and Biophysics* **31**: 19–48.

Ryan BM, Kirby JK, Degryse F, Harris H, McLaughlin MJ, Scheiderich K. 2013. Copper speciation and isotopic fractionation in plants: uptake and translocation mechanisms. *New Phytologist* **199**: 367–378.

Salt DE, Prince RC, Baker AJM, Raskin I, Pickering IJ. 1999. Zinc ligands in the metal hyperaccumulator *Thlaspi caerulescens* as determined using X-ray absorption spectroscopy. *Environmental Science & Technology* **33**: 713–717.

Savant NK, Snyder GH, Datnoff LE. 1997. Silicon management and sustainable rice production. *Advances in Agronomy* **58**: 151–199.

Smart KE, Smith JAC, Kilburn MR, Martin BGH, Hawes C, Grovenor CRM. 2010. High-resolution elemental localization in vacuolate plant cells by nanoscale secondary ion mass spectrometry. *Plant Journal* **63**: 870–879.

Sole VA, Papillon E, Cotte M, Walter P, Susini J. 2007. A multiplatform code for the analysis of energy-dispersive X-ray fluorescence spectra. *Spectrochimica Acta Part B-Atomic Spectroscopy* **62**: 63–68.

Song WY, Park J, Mendoza-Cozatl DG, Suter-Grotemeyer M, Shim D, Hortensteiner S, Geisler M, Weder B, Rea PA, Rentsch D *et al.* 2010. Arsenic tolerance in Arabidopsis is mediated by two ABCC-type phytochelatin transporters. *Proceedings of the National Academy of Sciences, USA* **107**: 21187–21192.

White PJ, Broadley MR. 2009. Biofortification of crops with seven mineral elements often lacking in human diets – iron, zinc, copper, calcium, magnesium, selenium and iodine. *New Phytologist* **182**: 49–84.

WHO. 2002. *World Health Report 2002. Reducing risks, promoting healthy life.* Geneva, Switzerland: World Health Organization.

Yamaguchi N, Ishikawa S, Abe T, Baba K, Arao T, Terada Y. 2012. Role of the node in controlling traffic of cadmium, zinc, and manganese in rice. *Journal of Experimental Botany* **63**: 2729–2737.

Yamaji N, Ma JF. 2009. A transporter at the node responsible for intervascular transfer of silicon in rice. *Plant Cell* **21**: 2878–2883.

Zhao FJ, McGrath SP, Meharg AA. 2010. Arsenic as a food chain contaminant: mechanisms of plant uptake and metabolism and mitigation strategies. *Annual Review of Plant Biology* **61**: 535–559.

Zhao FJ, Stroud JL, Khan MA, McGrath SP. 2012. Arsenic translocation in rice investigated using radioactive As-73 tracer. *Plant and Soil* **350**: 413–420.

Zheng LQ, Huang FL, Narsai R, Wu JJ, Giraud E, He F, Cheng LJ, Wang F, Wu P, Whelan J *et al.* 2009. Physiological and transcriptome analysis of iron and phosphorus interaction in rice seedlings. *Plant Physiology* **151**: 262–274.

Supporting Information

Additional supporting information may be found in the online version of this article.

Fig. S1 Annotated optical images of the internode region taken from an adjacent section to that analysed with high-resolution secondary ion mass spectrometry (NanoSIMS).

Fig. S2 Synchrotron X-ray fluorescence (S-XRF) colour merge image of the internode area shown in Fig. 2, showing variations in Mn, Zn and Fe in the fundamental parenchyma.

Fig. S3 High-resolution secondary ion mass spectrometry (NanoSIMS) images showing As and S highly localized in the companion cell vacuoles of an internode large vascular bundle.

Fig. S4 Graphs of mean S intensity vs mean As intensity from the companion cells of a diffuse vascular bundle, enlarged vascular bundle, leaf sheath vascular bundle and a small vascular bundle.

Fig. S5 High-resolution secondary ion mass spectrometry (NanoSIMS) images across the phloem region of a large vascular bundle from the internode showing the pairing of the companion cells and the sieve tubes and the cell wall localization of Cu.

Fig. S6 Annotated synchrotron X-ray fluorescence (S-XRF) image and corresponding stained optical image showing the morphology of the node.

Fig. S7 High-resolution secondary ion mass spectrometry (NanoSIMS) images showing the strong localization of Si in the cell walls between the fundamental parenchyma cells and the phloem of a diffuse vascular bundle.

Fig. S8 Synchrotron X-ray fluorescence (S-XRF) image of another node section showing the strong localization of Mn along the epidermal cells towards the top of the image.

Please note: Wiley Blackwell are not responsible for the content or functionality of any supporting information supplied by the authors. Any queries (other than missing material) should be directed to the *New Phytologist* Central Office.